J. Synchrotron Rad. (1998). **5**, 1375–1382

Calculation of Absolute Intensities From X-ray Imaging Plates

David J. Cookson

Australian Nuclear Science Technology Organization, Private Mail Bag 1, Menai, NSW 2234, Australia. E-mail: cookson@cars1.uchicago.edu

(*Received 7 May 1997; accepted 12 June 1998*)

A numerical technique for deriving a conversion factor between the output pixel values from a scanned imaging plate and the actual incident X-ray photon flux is proposed. The technique requires no external calibration by independent detectors, but uses the statistical information inherent in the image. As a test case, this technique was applied to a Fuji BAS2000 imaging-plate scanner. The calculation showed that, at 1.2 Å, 163 (8) photons pixel^{-1} were required to give one output unit of pixel intensity on an image scanned 20 min after exposure. This conversion factor compared favourably with the independently measured conversion factor of 171.1 (5) photons pixel^{-1} (output unit)$^{-1}$ obtained from a high-quantum-efficiency Ge detector.

Keywords: imaging plates; X-rays; images; statistics; intensity; calibration.

1. Introduction

Over the last ten years the imaging plate (IP) has become an important tool for X-ray data collection. It provides the experimenter with all the advantages of photographic film such as unlimited count rate and two-dimensional coverage. In addition to these benefits, the IP has a high quantum efficiency at hard X-ray energies, a large dynamic range, and is reusable. These qualities have made IPs popular when measuring X-ray intensities simultaneously over a comparatively large area of reciprocal space, especially in protein crystal diffraction and small-angle scattering experiments. More recently, the high count rate and sensitivity of IPs have been used to obtain short-exposure-time 'snap shots' of X-ray scattering patterns from samples undergoing physical or chemical changes (Amemiya *et al.*, 1988).

IPs use a photostimulable phosphor such as BaF(Br,I):Eu^{2+} where electrons excited from Eu^{2+} ions by an incident X-ray are trapped in a metastable state by Br^- and F^- vacancies, forming temporary 'colour centres' (Sonoda *et al.*, 1983). A trapped electron can be liberated from its metastable state *via* photostimulated luminescence (PSL). A latent image of colour centres generated from incident X-rays can be scanned with a focused red laser beam ($\lambda \simeq 632.8$ nm), producing blue ($\lambda \simeq 390$ nm) PSL photons which can then be detected with a photomultiplier tube (PMT). In this way, a virtual image of incident X-rays can be read, digitized and stored as an array of pixel intensities. Typically, an IP reader will be able to scan to a pixel size of about 100 μm. The spatial resolution is limited primarily by the scatter of red laser light within the IP matrix, which causes neighbouring pixels to partially fluoresce, adding some of their measurable intensity to the pixel being recorded. Recent developments have included the use of blue dyes in the IP matrix to minimize the laser light scatter and allow resolvable pixel sizes as small as 25 μm (Amemiya, 1995).

2. Measuring absolute intensity from imaging plates

Although the spatial resolution of an IP is adequate for a wide variety of X-ray scattering experiments (especially when using long sample-to-detector distances), some attention must be given to the accuracy and precision of the intensity values assigned to each pixel. The temporary colour centres decay spontaneously due to thermal relaxation, causing the latent image to fade with time after exposure (Mori *et al.*, 1994). The fading rate is independent of incident photon flux and energy (Amemiya, 1995) but changes with temperature and IP composition. In practice, although the fading rate can be well characterized for a given temperature and phosphor type, it is often difficult to scan IPs at a perfectly reproducible time. In addition to fading effects, individual scanners can differ in their calibration of output signal *versus* incident photon flux. This can happen even between scanners of identical make and model due to ageing of the scanning laser tube, for example.

One way of relating the scanner output to absolute incident X-ray intensity, without requiring external calibration and perfectly reproduced time intervals, would be to use the statistical information inherent in the scanned image. As the fading rate is independent of incident photon flux, the signal-to-noise ratio within an IP image should, to a good approximation, remain constant for at least a few hours between exposure and scanning.

© 1998 International Union of Crystallography
Printed in Great Britain – all rights reserved

On an ideal IP, where the pixel intensity output value, $I_{\rm out}$, is exactly proportional (with no instrumental or digitization noise) to an average incident irradiation of q_0 photons pixel^{-1}, the only fluctuation in neighbouring pixel intensities will be due to spatial variations of q_0 across the IP. If the incident photons came from some scattering event that obeyed Poisson statistics but was otherwise spatially uniform, the standard deviation of the fluctuations would be proportional to $q_0^{1/2}$. For such an IP the absolute intensity could be calculated from the output pixel value, $I_{\rm out}$, and the standard deviation of values across the pixels, $\sigma_{\rm out}$, using the equation

$$q_0 = (I_{\rm out}/\sigma_{\rm out})^2. \qquad (1)$$

In reality, although there is good linearity between the average incident X-ray flux and scanned pixel values (Miyahara *et al.*, 1986), every process element in the exposure and scanning of an IP is stochastic, and has either a binomial or Poisson nature (Amemiya *et al.*, 1988). Binomial processes include the absorption of the photons by the IP, the photostimulation of the colour centres, the collection of the blue photons and the emission of photoelectrons from the PMT photocathode. Poisson processes include the creation of the colour centres, and each successive stage of the cascade amplification of photoelectrons in the PMT. In addition to the necessary stochastic processes, there are also other unwanted elements that affect the fluctuation of measured intensity from pixel to pixel. These include creation of colour centres from cosmic rays, non-uniformity in IP composition, incomplete photostimulation of colour centres, non-uniformity in PSL collection, fluctuations of laser power and dark-current noise in the PMT. As a result, any attempt to model pixel variation against absolute incident X-ray intensity must allow for these effects.

Relating the actual pixel noise to the Poisson or 'shot' noise inherent in the input signal is an established technique for characterizing the performance of CCD imaging chips (Blouke *et al.*, 1983). For CCDs the noise *versus* signal curve has three regions: the 'read-noise' region at the low-signal end which defines the minimum 'dark-current' noise, the middle 'shot-noise' region dominated by the Poisson noise inherent in the input signal, and the high-signal region where small differences in sensitivity between individual pixels dominate. Although the detection processes at work in an imaging-plate system are quite different, some analogies can be drawn with CCDs when it comes to noise generation. An example of this is the 'dark current' of the PM tube in an IP system which behaves similarly to the 'read-noise' of a CCD chip, providing a baseline noise in the system. In IP scanners, systematic errors resulting from fluctuations in laser power, supply voltages and scanning geometries result in variations of effective detection efficiency from one pixel to another. This dominates the noise production at higher signal levels, not unlike the pixel sensitivity variations seen in CCDs. It should be noted, however, that while pixel-to-pixel differences in detection efficiency can be compensated for quite effectively in CCD images, this is only partially possible for IP images. IP pixel variations due to conditions that remain constant from one scanned IP to another (such as the scanning geometry) can be at least partially corrected for (Ito & Amemiya, 1991); however, this is not possible for transient variations in voltage and laser power fluctuations as well as inhomogeneities in IP composition.

3. Approximating the statistics of imaging-plate processes

For q_0 incident monochromatic photons on one IP pixel, the total number of photoelectrons, q_T, that eventually enter the final electronic amplifier (whose noise is negligible compared with fluctuations due to other elements in the system) can be written as (Amemiya *et al.*, 1988)

$$q_T = K\eta_4\eta_3\eta_2\kappa_1\eta_1 q_0, \qquad (2)$$

where κ_1 is the mean number of colour centres produced by the absorption of one X-ray photon (a Poisson stochastic elementary process) and η_j is the efficiency with which the jth binomial stochastic elementary process operates. The cascade amplification of photoelectrons is represented by K which, although made up of individual Poisson elementary processes, cannot be assumed to follow a Poisson distribution in its entirety. The total charge, q_T, results in a signal which is digitized with a finite resolution to a pixel value in a data memory array.

It can be shown (Akimov, 1965) that if a primary quanta (such as an absorbed X-ray) results in an average of κ secondary quanta, then for n primary quanta the relative variance (RV) in the total number of secondary quanta is given by

$$\mathrm{RV}(nk) = \sigma_{n\kappa}^2/\overline{(n\kappa)}^2 = \sigma_n^2/\overline{n}^2 + \sigma_\kappa^2/n\overline{\kappa}^2. \qquad (3)$$

The second term in this equation gives the amount of variance that is added to the variance of the input signal as a result of the cascade amplification. For energies above 5 keV, between 150 (Amemiya *et al.*, 1988) and 400 (Amemiya, 1995) colour centres will be produced by a single absorbed X-ray. This means that for the κ_1 process the cascade contribution to the noise will be negligible compared with the Gaussian noise resulting from inhomogeneities in colour-centre distribution and X-ray absorption. A similar argument can be applied to the photomultiplier stage where again the second term in (3) is made small, this time because n (the number of incident photoelectrons) is relatively large (Amemiya, 1995).

By justifiably neglecting the non-Gaussian noise generated by the cascade processes in the IP system we can approximate every stochastic process as a random variable with a Gaussian distribution. This way, although we have no detailed information regarding each separate process, it should be possible to model the fluctuations of output signal as a function of q_0 given actual intensity *versus* signal fluctuation data for a particular image. Using equation (2)

we can write, for the linearized output per pixel, $I_{\rm out}$, in PSL units,

$$I_{\rm out} = \gamma K \eta_4 \eta_3 \eta_2 \kappa_1 \eta_1 q_0 = \gamma A q_0, \qquad (4)$$

where γ is the scalar multiplier that converts the output current of the PMT into a linear pixel intensity value, and A represents the κ_1, K and η_i factors. For N independent random variables $(x_1 \ldots x_N)$ with standard deviations $(\sigma_1 \ldots \sigma_N)$, the product

$$f(x_1 \ldots x_N) = \prod_{i=1}^{N} x_i$$

will have a standard deviation given by

$$\sigma_f^2 = ({\rm d}f/{\rm d}x_1)^2 \sigma_1^2 + \ldots + ({\rm d}f/{\rm d}x_N)^2 \sigma_N^2. \qquad (5)$$

Using equations (4) and (5) and assuming q_0 obeys Poisson statistics (*i.e.* $\sigma_0^2 = q_0$), we obtain

$$\begin{aligned}\sigma_{\rm out}^2 &= \gamma^2 q_0 K^2 \eta_4^2 \eta_3^2 \eta_2^2 \kappa_1^2 \eta_1^2 + \gamma^2 q_0^2 [\sigma_K^2 \eta_4^2 \eta_3^2 \eta_2^2 \kappa_1^2 \eta_1^2 + \ldots] \\ &= \gamma^2 q_0 A^2 + \gamma^2 q_0^2 B, \qquad (6)\end{aligned}$$

where $B = \sigma_{K_{\kappa\eta}}^2$ can be thought of as the combined variance of all the stochastic processes linking one incident X-ray photon to a number of photoelectron pulses from the PMT. If we assume that the standard deviation of each binomial process will scale linearly with q_0, then A and B become parameters that we can fit to actual IP data. Background noise caused by such random processes as power supply fluctuations, cosmic rays and dark currents can be represented by Gaussian distributions with fixed standard deviations to give the following numerical model,

$$I_{\rm out} \simeq \gamma\big[(q_0 A^2 + q_0^2 B)^{1/2} \mathbf{G}_1 + c\mathbf{G}_2\big], \qquad (7)$$

where $\mathbf{G}_1$ and $\mathbf{G}_2$ are independently generated sets of normally distributed random numbers with a mean of zero and a standard deviation of unity. The $\mathbf{G}_1$ term represents the noise resulting from the amplification processes while the $\mathbf{G}_2$ term represents the baseline noise sources such as PMT dark current.

Using a 'Monte Carlo'-style approach when dealing with noise generation in imaging devices is not new. In work performed more than a decade ago, the phenomena of charge-splitting between pixels in CCD chips was modelled using random number simulations (Janesick *et al.*, 1987) where the trajectories of individual photoelectrons were followed through the bulk of a CCD pixel array. Our work has a qualitative similarity to these models in that the progress of quanta are traced using random number generation. Our model differs in that it follows individual quanta through a conceptual space made of independent stochastic processes rather than some real physical space. Other ways of characterizing imaging devices from the image statistics have been reported more recently (Dufresne *et al.*, 1995; Zannella & Zannoni, 1996). These methods, however, concentrate more on detector performance rather than calibration.

Of considerable importance when considering the statistical fluctuation of pixel values is the point spread function (PSF) in two dimensions. In a CCD chip, a narrow PSF profile results in a high pixel resolution. Unfortunately, this has to be traded against efficiency of charge transfer (Allinson, 1989) which will often compromise the detective quantum efficiency (see §10) of each pixel. A similar trade-off also holds true for imaging-plate systems, where effective collection of PSL entails a certain amount of cross-talk between pixels, depending on the scanning optics and scatter of the laser (Amemiya *et al.*, 1988). This cross-talk will have the effect of smoothing out fluctuations between neighbouring pixels. The smoothing process can be simulated using some profile $\mathbf{P}$ to approximate the PSF which, when convoluted with $\mathbf{G}_1$, effectively reduces its standard deviation, giving

$$I_{\rm out} \simeq \gamma\big[(q_0 A^2 + q_0^2 B)^{1/2} \mathbf{G}_1 \otimes \mathbf{P} + c\mathbf{G}_2\big]. \qquad (8)$$

As the degree of cross-talk between pixels is represented by the width of the PSF, the choice of a realistic profile for $\mathbf{P}$ is crucial for a successful numerical model.

4. Digitization of pixel values

Assuming that the logarithmic amplifier is effectively noiseless with respect to all the other processes taking place in the scanner, the actual binary integer value obtained for each pixel as a result of digitization in the BAS2000 IP scanner is given by the binary pixel value, $I_{\rm bin}$, where

$$I_{\rm bin} = {\rm Integer}\big\{(2^N/L)\big[\log_{10}(SI_{\rm out}/4000) + L/2\big]\big\}, \qquad (9)$$

where 'Integer{ ... }' means the integer part of { ... }, S is the scanning sensitivity, L is the scanning latitude and N is the number of bits used for digitization (8 or 10). In the BAS2000 scanner, the integer range of $I_{\rm bin}$ is 0–255 for 8-bit resolution or 0–1023 for 10-bit resolution. It should be noted that this equation shows how the scanning parameters affect the digitization for the BAS2000 scanner, and would not necessarily hold true for other scanners. One

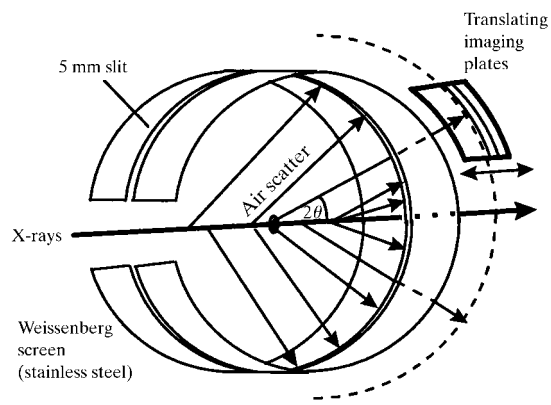

Figure 1
Experimental configuration, showing how the IP is masked from the air scatter by a stainless-steel Weissenberg screen. Uniform exposure in each strip is achieved by translating the IP at a uniform rate past the slit.

virtue of this particular conversion formula is that $I_{\rm out} = 1.0$ always represents the middle of a digitization range defined by S and L.

If we momentarily disregard the 'integer part of' operator in equation (9) and allow the function to vary continuously, its gradient can be written

$$\mathrm{d}I_{\rm out}/\mathrm{d}I_{\rm bin} = I_{\rm out}(L/2^N)\ln 10. \qquad (10)$$

Using this gradient we can determine that the resolution of digitization should give rise to an additional component of random noise with a variance $\sigma^2_{\rm dig}$ given by

$$\sigma^2_{\rm dig} = \int_0^{1/2} \left[(\mathrm{d}I_{\rm out}/\mathrm{d}I_{\rm bin})I'\right]^2 \mathrm{d}I' = (1/12)(\mathrm{d}I_{\rm out}/\mathrm{d}I_{\rm bin})^2, \qquad (11)$$

and hence a standard deviation, $\sigma_{\rm dig}$, given by

$$\sigma_{\rm dig} = I_{\rm out}\left[(12)^{-1/2}(L/2^N)\ln 10\right] \propto I_{\rm out}. \qquad (12)$$

This noise term, like the B term in equation (6), increases linearly with the output signal, and could be easily incorporated as an explicit term in the model. In this work, however, the digitization noise was simulated numerically by using equation (9) to convert intensities generated from equation (8) to rounded binary logarithmic integers, and then back again to linear floating-point values. This allowed us to model both the digitization noise and the effect of approaching the extremes of the digitization range.

5. Experimental method – collection of imaging-plate data

To obtain IPs with sufficiently large regions of uniform irradiation, the Australian diffractometer (Barnea *et al.*, 1992) was used with a Weissenberg screen and a translatable IP holder as shown in Fig. 1. Air scatter was used with a monochromatic ($\lambda = 1.2$ Å) X-ray beam to give a range of incident X-ray intensities most intense at $2\theta = 0$, decreasing with increasing 2θ. Fig. 2 shows an IP image with three strips of exposure. Along the 2θ (long axis) direction of each strip the degree of exposure smoothly varied while the irradiation perpendicular to this was nominally uniform within each strip. A wavelength of 1.2 Å was chosen because it lay in the energy region below the Br K edge (1.04 Å) where the Fuji IP shows its greatest sensitivity.

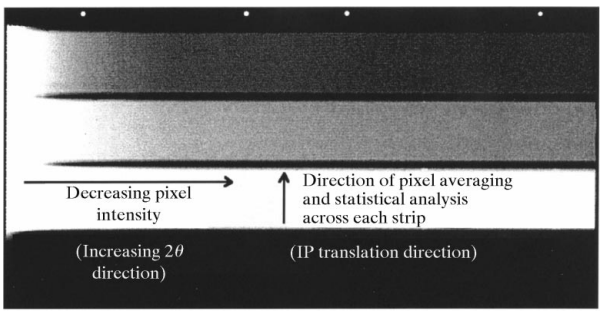

Figure 2
IP showing irradiated strips of smoothly varying intensity in the long axis and uniform intensity across the width of each strip. Irradiation wavelength = 1.2 Å.

Uniformity of exposure was achieved by translating the IP past the 5 mm Weissenberg slit in steps of 0.1 mm. At each step, the IP was held for a fixed number of monitor counts to compensate for the effect of intensity decay in the synchrotron beam. Each of the three strips on the IP represented a different number of monitor counts per translation step, in order to cover as wide a range of integrated irradiation intensities as possible. After 20 min exposure, each plate was scanned. As any model of pixel value *versus* incident X-ray intensity would have to be valid for an arbitrary set of scanning parameters, a number of IPs were exposed and scanned with a variety of sensitivity, latitude and bit resolution (S, L and N) combinations on the Fuji BAS2000 scanner.

6. Data extraction from imaging plates

Each exposed strip in Fig. 2 had a width in the translation direction of 400 pixels and a length in the 2θ direction of 4000 pixels. To avoid edge effects, a width of 50 pixels was discarded from the top and bottom edges of each strip, reducing the effective strip width to 300 pixels in the translation direction. Prior to averaging and statistical analysis, every pixel on the IP was converted from a binary integer to a linear floating-point number using the inverse of equation (9).

After conversion to linear floating-point numbers, each strip yielded 4000 columns of 300 pixel intensity values from which 4000 means and standard deviations were calculated. In this way, each IP produced a set of 12 000 pixel intensity *versus* intensity fluctuation data points. Fig. 3 shows σ_I/I (also known as the relative standard deviation or RSD) plotted against intensity I from one IP data set. The straight dashed line represents the theoretical RSD of an ideal detector described by equation (1). Note that the 'ideal detector' was given an arbitrary scaling factor of 1 PSL unit per 300 incident X-rays.

An additional problem arose from the fact that although the initial irradiation of each strip was transversely uniform, the length of time between exposure and scanning varied continuously across each strip in the translation direction. This resulted in a discernible slope on what should have otherwise been a flat intensity profile. To prevent this from erroneously increasing the measured standard deviation of pixel intensities, each column profile was flattened with a second-order polynomial, preserving the higher-frequency statistical noise.

7. Determining the PSF of the imaging plate and scanner

It is theoretically possible to effectively determine what the 'real' pixel variances would be without the smoothing effect of a PSF using spatial autocorrelation functions. This has been performed successfully for real CCD data (Dufresne

et al., 1995), and eliminates the need to separately determine the PSF. Unfortunately, in order to obtain good statistics this method requires thousands of evenly irradiated pixels, impractical for IPs where large pixel sizes and image fading make the homogeneous irradiation of many pixels relatively difficult. Thus, for our purposes, an independent determination of the PSF was necessary.

To calculate the PSF in the direction of pixel averaging, a single IP was exposed with a sharp shadow produced by a straight edge of lead in contact with the IP, running along the 2θ direction. The Lorentzian profile which gave the best approximation of the resulting edge image when convoluted with a step function was taken to be the PSF in the pixel-averaging direction (Fig. 4). From this analysis the FWHM of the Lorentzian of best fit was found to be 1.26 (2) pixels. Direct measurement of the PSF profile by previous authors (Bourgeois *et al.*, 1994) gave an experimental FWHM of 1.42 (5) pixels and a FW@0.1% of 11.1 (5) pixels at 1.2 Å. This implied that our Lorentzian profile approximation to the true PSF was reasonable.

To check further this estimation of the PSF width, a Fourier transform was calculated for each column of pixel intensities and averaged over all the columns in a strip (Fig. 5). If the pixel intensity fluctuations in each column were truly random, the average normalized power spectrum would be flat as shown by the dashed line in Fig. 5. Convoluting pseudo-randomly generated pixel intensities with Lorentzian PSFs of different width would result in transform profiles as shown by the solid curves. In general, the experimental data deviates markedly from all of these curves but, at the highest spatial frequency of 0.5 pixel^{-1}, shows reasonable agreement with the theoretical curve derived from a 1.26 pixel FWHM Lorentzian. As the primary purpose of the Lorentzian in our model was to simulate the suppression of the higher-frequency pixel fluctuations, this was seen as further confirmation that an appropriate PSF had been chosen for the numerical model. An explanation for the shape of the curve derived from the experimental data may lie in the algorithm used by the BAS2000 scanner to compensate for optical distortions caused by the scanning geometry (Ito & Amemiya, 1991).

8. Fitting of numerical model parameters

To reduce computing time, all sets of intensity *versus* intensity fluctuation data were condensed from 2000 separate points to 100 points with associated error bars. Each of the condensed points was an average of all the points lying within its proximity on the intensity axis. Fig. 3 shows a high density of data points in the low-intensity region which become scarcer at higher values of pixel intensity. As a result, the condensed data points at low values of pixel intensity could represent an average of hundreds of measured data points while those located further along the intensity axis may only represent a few. Thus the error bar associated with each condensed data point reflects not only the scatter of all the averaged points but the number of points in each average.

The numerical fitting was achieved using a program written in the image-processing language IDL (Research Systems Inc., 1995). Equations (6), (8) and (9) formed the basis of the program, where 300 element vectors of pseudo-randomly generated normally distributed floating-point numbers were used for $\mathbf{G}_1$ and $\mathbf{G}_2$. Two new vectors for $\mathbf{G}_1$ and $\mathbf{G}_2$ were generated at every intensity for which the model was calculated. Each sub-plot in Fig. 6 shows the experimental values of σ_I/I (RSD) *versus* I for a different strip-exposed IP using different BAS2000 scanning parameters (S, L and N). The solid lines show the RSD *versus* I relationships calculated from the numerical model using the four fitted parameters. The dashed line in each sub-plot shows the behaviour of the same ideal detector shown in Fig. 3.

In this model the A and γ parameters are highly correlated, so in order for the refinement to proceed, a number of values of A were chosen in the range 100–500 while the γ, B and C parameters were allowed to vary for a best fit.

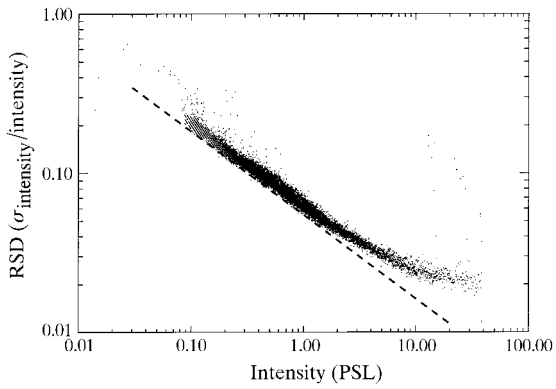

Figure 3
Plot of pixel RSD *versus* pixel intensity for one scanned IP using a BAS2000 scanner with S = 4000, L = 3 and N = 8. Dashed line shows RSD *versus* I for an 'idealized' IP system with a scaling factor of 300 X-ray photons per PSL unit.

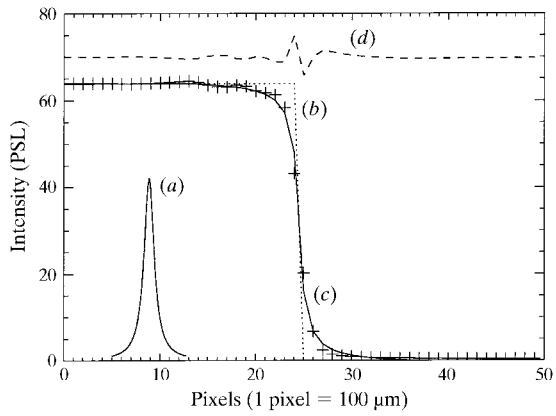

Figure 4
(*a*) Lorentzian PSF (FWHM = 1.26 pixels) convoluted with step function (*b*) to give a best fit (*c*) of the experimental edge profile shown by crosses. Curve (*d*) shows the error between data and profile of best fit.

Table 1
Fitted parameters for numerical model relating pixel intensity to pixel intensity noise.

The asterisk marks the row containing parameters of best fit.

A	γ	B	C	γA	R
100	0.000092 (5)	3.0 (5)	0.016 (1)	0.0092 (11)	0.803
200	0.000045 (3)	6.0 (5)	0.015 (1)	0.0090 (11)	0.764
*300	0.000031 (2)	8.0 (7)	0.015 (1)	0.0092 (11)	0.741
400	0.000022 (1)	12.0 (8)	0.015 (1)	0.0088 (11)	0.765
500	0.000018 (1)	15.0 (8)	0.017 (1)	0.0090 (11)	0.794

Table 1 shows these values and the associated R-factor for each fit. It is important to stress that for the purposes of this investigation the fitted value for A was not as important as the product γA. In this work, A was chosen to be 300 (based on the R value) while the value of γA which gave the best fit to experimental data was found to be 0.009 (1) PSL units per photon. This number can be thought of as the linear conversion factor between incident X-ray photons and PSL output *immediately after exposure*. As there will always be some image fading before the IP can be scanned, it is necessary to use the curves shown in Fig. 6 to convert an observed RSD from the IP image to an equivalent 'immediately scanned' or '$t = 0$' PSL value. The method for obtaining an absolute X-ray calibration on a previously scanned IP can be summarized as follows: (*a*) measure the average RSD in some 'evenly' exposed region on the IP image; (*b*) convert the measured RSD to a '$t = 0$' PSL value using the fitted RSD *versus* PSL curves; (*c*) divide the '$t = 0$' PSL value by the fitted value of γA to give the 'true' X-ray count for that region; (*d*) scale the entire image to the analyzed region, assuming a linear IP response.

9. Comparison of absolute imaging-plate intensities with a single-photon counter

As a final check of the efficacy of the IP calibration procedure described in the previous section, a single-photon counting detector was used to provide a separate IP calibration check at a single X-ray energy.

Using a Camberra germanium detector with no energy discrimination, the fluorescence from a copper foil placed in the path of a monochromatic (1.2 Å) X-ray beam was measured for approximately 1 min (18000 monitor pulses) at a distance of 180 mm. This distance was chosen to ensure that the total detector count rate was kept below 10000 counts s^{-1} in order to preserve linearity and keep the quantum efficiency close to 100%. Over a period of 1 min, the average count collected by a detector surface area of 100 × 100 µm was 40.9 (1) photons.

After counting to a fixed number of incident beam monitor counts, the detector was replaced by an IP at the same distance from the fluorescence source and exposed for an identical number of monitor pulses (~1 min). 20 min after the exposure, the IP was scanned ($S = 4000$, $L = 3$, $N = 10$) and the average pixel intensity and intensity fluctuation were calculated over the area corresponding to the former position of the Ge detector. The average intensity in this image region was found to be 0.239 PSL units with a standard deviation of 0.0247 PSL units, yielding an RSD value of 0.103. This corresponded to a '$t = 0$' RSD of 0.32 (2) which, when divided by γA, gave an absolute intensity of 39 (2) X-rays per 100 × 100 µm pixel. This compared well with the absolute X-ray count obtained from the Ge detector.

The calibration for this particular image was therefore 163 (8) incident X-rays per PSL unit. This calibration factor would also apply to other IP images as long as they were allowed to fade for 20 min at the same ambient temperature prior to scanning on the same scanner. Images with different fading times could be calibrated using the same fitted curves assuming a reliable RSD value could be determined from some area of the image. For different scanners using similar transport and optics it should be possible to use the same model with different fitted parameters. All that would be required is a representative range of pixel intensity *versus* pixel fluctuation data and some knowledge of the pixel PSF.

10. Detective quantum efficiency

The detective quantum efficiency (DQE) is a fundamental measure of detector quality that can be used to specify detector characteristics at various dose rates (Gruner *et al.*, 1978). It is defined by the equation

$$\mathrm{DQE} = \frac{(\text{output signal/output noise})^2}{(\text{input signal/input noise})^2}, \qquad (13)$$

where an ideal detector will have a DQE of unity over all count rates. The numerator of equation (13) can be obtained directly from the curves shown in Fig. 6 while the denominator depends on the final calibration, which in turn

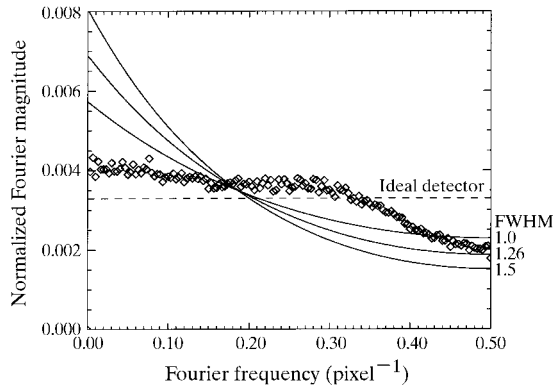

Figure 5
Fourier transform of pixel fluctuation noise from a uniformly irradiated area on a BAS2000 IP. Diamonds indicate experimental data, solid lines represent the transforms of theoretical fluctuation noise obtained by convoluting numerically generated noise with Lorentzian profiles of differing widths (FWHM = 1.0, 1.26, 1.5). All transform profiles have been normalized to bound equal areas.

depends on the length of time between IP exposure and scanning. For the IP images used in this study (20 min delay between exposure and scanning), some derived DQE *versus* incident count rate curves are shown in Fig. 7.

In general, the DQE curves calculated from the numerical model showed little variation for different combinations of S, L and N. The greatest discernible difference seen was between the DQE curves calculated for 10-bit resolution (solid line) and 8-bit resolution (dashed line), both calculated at the maximum sensitivity (S = 10000) and latitude (L = 4). The calculated DQE curves show reasonable agreement with experimental values (points) and also bear a good qualitative resemblance to experimentally derived DQE data published by previous authors (Amemiya, 1995).

For shorter time lags between exposure and scanning, these curves would be unchanged in shape, but would have maxima closer to unity. The DQE of an IP system decreases with increasing fading time due to the reduction of active colour centres that can be stimulated. This is conceptually equivalent to putting an absorber in front of the detector (Zannella & Zannoni, 1996), which effectively changes the signal-to-noise ratio of the input signal without affecting the noise-adding processes taking place inside the detector system.

It would seem to be a good idea to minimize the delay time between the exposure and scanning of IPs, to maximize the effective DQE. This is primarily limited by the undesirable possibility of the latent image fading significantly during the scanning process, which typically takes 2–3 min to complete. Approximately 15–30 min provides a reasonable compromise between these requirements, although scanning IPs some hours after exposure usually results in perfectly useable images.

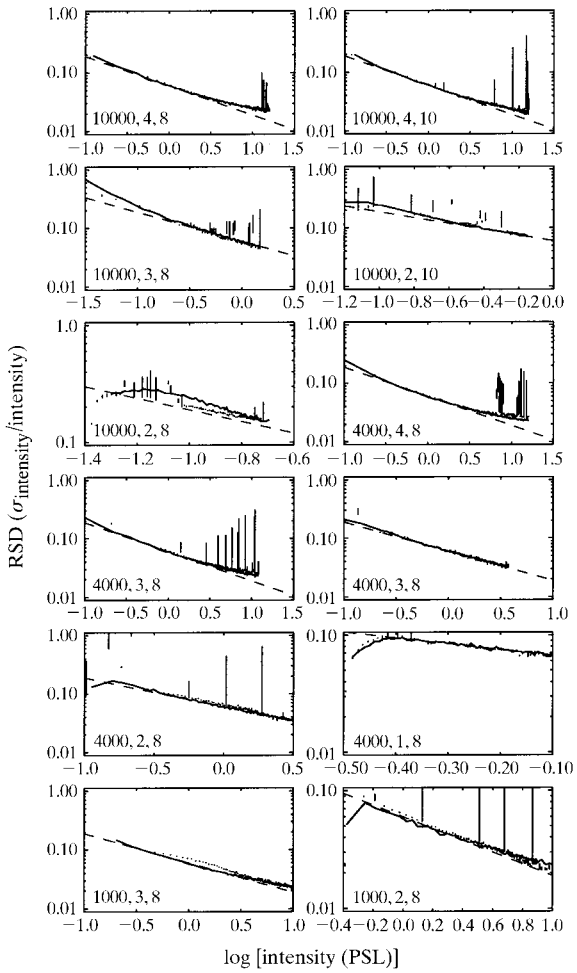

Figure 6
Comparison of numerical model (solid lines) using parameters of best fit (A = 300, B = 8, C = 0.015 and γ = 0.000031) with experimentally obtained RSD values (vertical bars with length = estimated error). Each sub-plot represents data measured and fitted using the S, L and N BAS2000 scanning parameters shown in the bottom left-hand corner of each sub-plot. The dashed line on each sub-plot represents the behaviour of an 'ideal' IP detector with a scaling factor of 300 X-ray photons per PSL output unit.

11. Conclusions

Using the Australian National Beamline Facility's BAS2000 IP scanner with Fuji IPs, and a 20 min delay between IP exposure and scanning, the formula for converting PSL units to incident X-ray photons was found to be

$$\text{incident photons} = 163\,(8) \times I_{\text{out}},$$

where I_{out} is given in BAS2000 PSL units. This compared well with a conversion factor of 171.1 (5) obtained by using an independent single-photon counting detector.

Using the numerical model described in this work with the same four fitted parameters, it is practical and straightforward to derive a conversion factor for any IP scanned at some arbitrary time after exposure on this machine, using only the statistical data inherent in the image. Furthermore, this numerical model with a different set of four fitted parameters should be applicable to other scanners using similar optics and transport mechanisms,

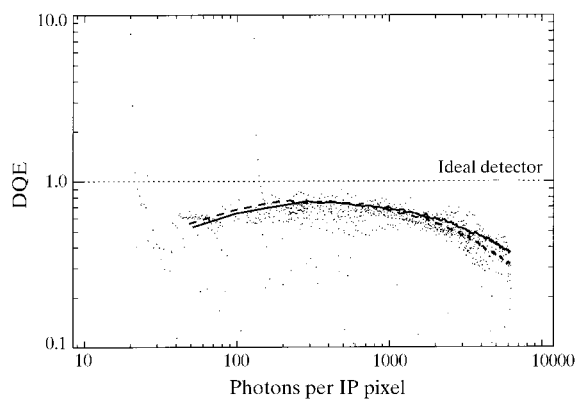

Figure 7
Experimentally obtained DQE *versus* incident X-ray photon count for IPs (dots) using a range of scanning parameters. The DQE calculated from the numerical model is given by the thick solid line (S = 10000, L = 4 and N = 10) and the thick dashed line (S = 10000, L = 4 and N = 8). An ideal detector would have a DQE of unity for all incident photon count rates.

given sufficient knowledge of the system's point spread function.

Many thanks to Professor Y. Amemiya for a number of useful discussions regarding imaging-plate technology and theory. Thanks also to my colleague Dr Garry Foran for his assistance and support at the Australian beamline. This work was supported by the Australian Synchrotron Research Program which has been funded by the Commonwealth of Australia *via* the Major National Research Facilities Program.

References

Akimov, Yu. K. (1965). *Scintillation Counters in High-Energy Physics*, pp. 32–35. New York: Academic Press.

Allinson, N. M. (1989). *Nucl. Instrum. Methods*, A**275**, 587–596.

Amemiya, Y. (1995). *J. Synchrotron Rad.* **2**, 13–21.

Amemiya, Y., Matsushita, T., Nakagawa, A., Satow, Y., Miyahara, J. & Chikawa, J. (1988). *Nucl. Instrum. Methods*, A**266**, 645–653.

Barnea, Z., Creagh, D. C., Davis, T. J., Garrett, R. F., Janky, S., Stevenson, A. W. & Wilkins, S. W. (1992). *Rev. Sci. Instrum.* **63**, 1069–1072.

Blouke, M. M., Janesick, J. R., Hall, J. E., Cowens, M. W. & May, P. J. (1983). *Opt. Eng.* **22**, 607–614.

Bourgeois, D., Moy, J. P., Svensson, S. O. & Kvick, A. (1994). *J. Appl. Cryst.* **27**, 868–877.

Dufresne, E., Bruning, R., Sutton, M., Rodricks, B. & Stephenson, G. B. (1995). *Nucl. Instrum. Methods*, A**364**, 380–393.

Gruner, S. M., Milch, J. R. & Reynolds, G. T. (1978). *IEEE Trans. Nucl. Sci.* **25**, 562–565.

Ito, M. & Amemiya, Y. (1991). *Nucl. Instrum. Methods*, A**319**, 369–372.

Janesick, J. R., Elliot, T., Collins, S., Daud, T. & Campbell, D. (1987). *Opt. Eng.* **26**, 156–166.

Miyahara, J., Takahashi, K., Amemiya, Y., Kamiya, K. & Satow, Y. (1986). *Nucl. Instrum. Methods*, A**246**, 572–578.

Mori, C., Matsumura, A., Suzuki, T., Miyahara, H., Aoyama, T. & Nishizawa, K. (1994). *Nucl. Instrum. Methods*, A**339**, 278–281.

Research Systems Inc. (1995). *IDL Reference and User Guides.* Research Systems Inc., Colorado, USA.

Sonoda, M., Takano, M., Miyahara, J. & Kato, H. (1983). *Radiology*, **148**, 833–838.

Zannella, G. & Zannoni, R. (1996). *Nucl. Instrum. Methods*, A**381**, 157–160.